

Upgrade of beamline BL08B at Taiwan Light Source from a photon-BPM to a double-grating SGM beamline

Jih-Young Yuh,^{a*} Shan-Wei Lin,^a Liang-Jen Huang,^a Hok-Sum Fung,^a Long-Life Lee,^a Yu-Joung Chen,^b Chiu-Ping Cheng,^c Yi-Ying Chin^a and Hong-Ji Lin^a

Received 29 May 2015

Accepted 23 July 2015

Edited by J. F. van der Veen

Keywords: extreme ultraviolet (EUV); soft X-rays; spherical-grating monochromator (SGM) beamline; Taiwan Light Source; photon beam-position monitor (BPM).

Supporting information: this article has supporting information at journals.iucr.org/s

^aNational Synchrotron Radiation Research Center, 101 Hsin-Ann Road, Hsinchu Science Park, Hsinchu 30076, Taiwan,

^bDepartment of Physics, National Central University, 300 Jhongda Road, Jhongli, Taoyuan 32054, Taiwan, and

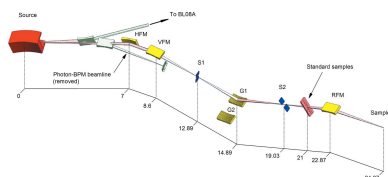
^cDepartment of Electrophysics, National Chiayi University, 300 Syuefu Road, Chiayi 60004, Taiwan.

*Correspondence e-mail: jyyuh@nsrrc.org.tw

During the last 20 years, beamline BL08B has been upgraded step by step from a photon beam-position monitor (BPM) to a testing beamline and a single-grating beamline that enables experiments to record X-ray photo-emission spectra (XPS) and X-ray absorption spectra (XAS) for research in solar physics, organic semiconductor materials and spinel oxides, with soft X-ray photon energies in the range 300–1000 eV. Demands for photon energy to extend to the extreme ultraviolet region for applications in nano-fabrication and topological thin films are increasing. The basic spherical-grating monochromator beamline was again upgraded by adding a second grating that delivers photons of energy from 80 to 420 eV. Four end-stations were designed for experiments with XPS, XAS, interstellar photoprocess systems (IPS) and extreme-ultraviolet lithography (EUVL) in the scheduled beam time. The data from these experiments show a large count rate in core levels probed and excellent statistics on background normalization in the *L*-edge adsorption spectrum.

1. Introduction

In 1994 the first beamline of Taiwan Light Source (TLS) was installed (BL08A; Tseng *et al.*, 1995). A photon-BPM (former position indicated in Fig. 1) was concurrently set up as side-branch beamline BL08B, which provided important information about the stability of the photon beam and details of perturbations in the storage ring. After operation for a decade, the number of beamlines in TLS has attained its maximum capacity. In 2007 the photon-BPM was removed; our original plan was to build a testing beamline for R&D of synchrotron optics. After the development of a project on an active-grating monochromator was completed (Fung *et al.*, 2007), the beamline was redesigned for scientific purposes. To simplify the construction of the monochromator chamber only a single spherical grating for 300–1000 eV was included; since that time, BL08B has competently relieved the heavy beam-time loading from other soft X-ray beamlines in the facility. This beamline has provided photons to probe novel materials such as spinel oxides and organic light-emitting device materials. Fruitful information can be extracted in experiments using core-level XPS and *L*-edge XAS, but responding to growing demands for application to environmental materials, interstellar chemistry and extreme-ultraviolet lithography (Thomas *et al.*, 2010) we decided to upgrade the monochromator by adding an extra grating and a new three-slot grating chamber. The range of BL08B currently extends to the extreme ultraviolet (EUV) range, which delivers photons of energy from 80



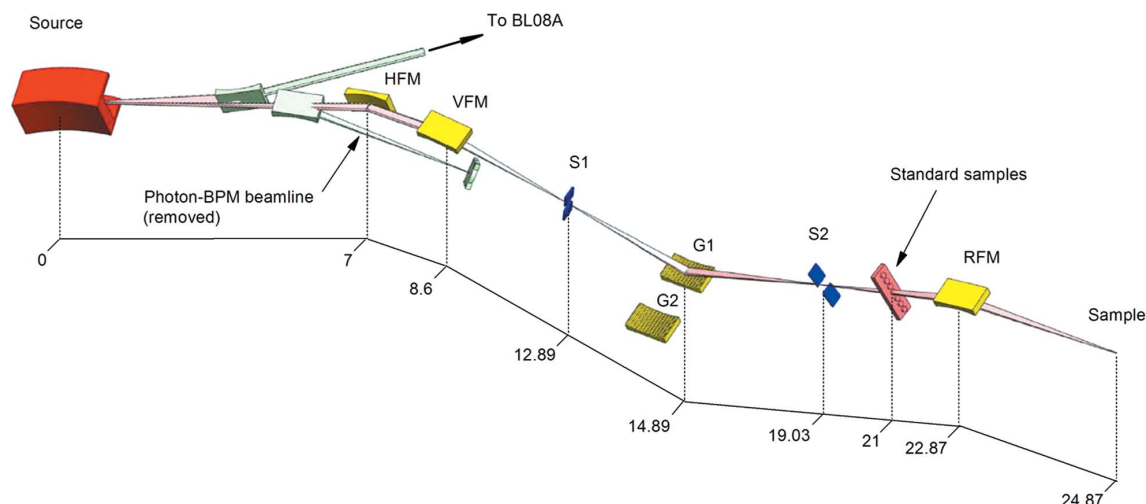


Figure 1
Schematic diagram of beamline 08A, B and photon-BPM (before removal).

to 1200 eV; the photon flux has attained 7×10^{11} photon s^{-1} and resolving power $>10\,000$ at 400 eV. Three advanced UHV chambers consumed most beam time on a cyclical basis: XPS end-station, XAS end-station and an interstellar photoprocess systems (IPS) end-station, with a fourth end-station (compact reflectometer) in preparation. Benefiting from the top-up mode and the highly stable operation at TLS, the experimental data showed a reasonable count rate, excellent statistics and a smooth background after normalization. In the future, the remaining slot of the grating chamber will be occupied either with a new grating for another energy range or to serve as a metrology beamline for advanced synchrotron optics.

2. Beamline overview

To take advantage of the minimum number of optical elements between the fixed entrance slit and the movable exit slit, the BL08B beamline adopts a Dragon-type spherical-grating monochromator (SGM) design (Chen & Sette, 1989). Beyond the design objectives of high resolution and great flux density in the range of photon energy from the VUV to soft X-ray, the beamline is more convenient for users considering its luxurious working space and convenience of beamline diagnostics compared with other SGM beamlines in TLS. Fig. 1 shows a schematic diagram of the beamline layout. The bending-magnet source has divergence angles of 40 mrad horizontal and 5 mrad vertical. The source was split into 14 mrad and 8.5 mrad for BL08A and BL08B, respectively. The latter was deflected with a horizontal focusing mirror (HFM) with included angle $2\theta = 174^\circ$. The plane elliptical HFM is intermediately focused horizontally at 13.6 m downstream; the large heat load on the mirror was effectively relieved with a sideways water-cooling system. The vertically focused mirror (VFM) has a cylindrical shape, with included angle $2\theta = 176.5^\circ$; the beam is deflected downward with demagnification 2:1 at the entrance slit. This slit is also water-cooled to decrease the effect of thermal instability on the defined source point on the grating. In a Dragon-type design, the focusing condition is fulfilled with a variable included

angle and a movable exit slit. Two spherical gratings (350 and 1000 grooves mm^{-1}) cover energy ranges 80–420 eV and 350–1200 eV, respectively. The moving range of the exit slit is ± 35 cm. Before entry into the refocusing-mirror (RFM) chamber, single-crystal oxide samples in a series can be selected for calibration of photon energy during an experiment. The photon beam is weakly converging with a toroidal RFM at an incident angle of 88.25° and a distance of 1.454 m parallel to the ground floor. All optical elements in this beamline are kinematically mounted on a x - y - z precision stage (developed by the beamline group at TLS) for fine adjustment. The final focal position at the sample is 2 m from the center of the RFM, which provides sufficient space to accommodate various end-stations. Note that all optics are gold-coated and that the detailed design parameters are listed in Table 1.

The grating chamber contains two gratings (350 and 1000 grooves mm^{-1} ; Horiba Jobin Yvon); its vacuum vessel and mechanical parts were manufactured locally and tested at the TLS. The basic design concept (Hulbert *et al.*, 1990) of the scanning mechanism consists of a grating-holding cradle connected at its center of rotation with the upper end of a sine arm; the other end is pushed with a rod fixed at a scanning stage with a scan range of 3° and a step resolution of 0.2 μrad . The base plate of the cradle is seated on three adjustable kinematic mounts. The rotation axis (grating pole) is precisely aligned with a theodolite to ensure its height and orthogonality relative to the beam direction. The sine arm is driven with a precise linear stage (Micos, UPM-160) *via* a 4:1 gear, lead screw (10 pitch per inch), which results in an overall resolution of 5 nm. A counterbalanced weight was added to minimize the vibration of the cantilever pendulum so that the weight on the grating holder would be balanced. Other special features of the beamline are six oxide single-crystal samples, *i.e.* SrTiO₃, MnO, Fe₂O₃, CoO, NiO and CuO, vertically mounted at a linear feedthrough to provide real-time energy calibration during XAS experiments (see bottom of Fig. 4), and a compact photon-energy beamline diagnostic tool for routine verification of the beamline performance. In brief, the differentially

Table 1
Description of the optical components.

Optical element	Distance (m)	Included angle (r_1, r_2)	Description
Source	0		Bending magnet, $E = 1.5$ GeV, $I = 360$ mA, Divergence 8.5 mrad
HFM	7	174° (7 m, 13.6 m)	Plane elliptical, $a = 10.3$ m, $b = 0.51$ m, water-cooled, Si-substrate Au-coated, 1200 mm × 70 mm × 50 mm
VFM	8.6	176.5° (8.6 m, 4.3 m)	Cylindrical, $R_{\text{tan}} = 187.74$ m, 700 mm × 75 mm × 70 mm, Si-substrate Au-coated
Entrance slit	12.89		Water-cooled, 2 μm –1 mm adjustable
G1 (1000 lines mm^{-1})	14.89	173° (2 m, 4 m)	Spherical, $R = 49.28$ m, 180 mm × 30 mm × 50 mm, fused silica substrate Au-coated
G2 (350 lines mm^{-1})	14.89	173° (2 m, 4 m)	Spherical, $R = 49.28$ m, 180 mm × 30 mm × 50 mm, fused silica substrate Au-coated
Exit slit	19.03		Travel distance ± 35 cm
Standard samples	~21		Single crystal NiO, SrTiO ₃ , MnO, Fe ₂ O ₃ , CoO, CuO
RFM	22.87	176.5° (4 m, 2 m)	Toroidal, $R = 87.32$ m, $\rho = 65$ mm, 700 mm × 60 mm × 70 mm, Zerodur substrate Au-coated
Beam size at 400 eV	24.87		<0.5 mm × 2 mm (V × H)

pumped windowless ion chamber and the flux-measurement chamber measure energy resolution, flux and beam size of the photon beamline consecutively with a photo-diode or gold mesh (Wei *et al.*, 2015). The beamline is operated with two simple routines controlled with the *Labview* program; the photon flux of the zero-order beam is optimized by automatically adjusting the VFM to a position with maximum flux. The first-order photon energy is selected on concurrently scanning the grating angle and translating the exit slit. The safety of the beamline is constantly monitored with an interlock system based on a programmable logic control and a flat-panel display (32 inch) that constantly updates the operational status (vacuum, pumps, gate valves, *etc.*). Any abnormal condition of the beamline raises an alarm and is logged for failure analysis.

3. Beamline performance

Fig. 2 shows the photon flux measured with a photo-diode (IRD AXUV 100) at the final focal position, with widths of entrance and exit slits set at 50 μm . The photo-current was

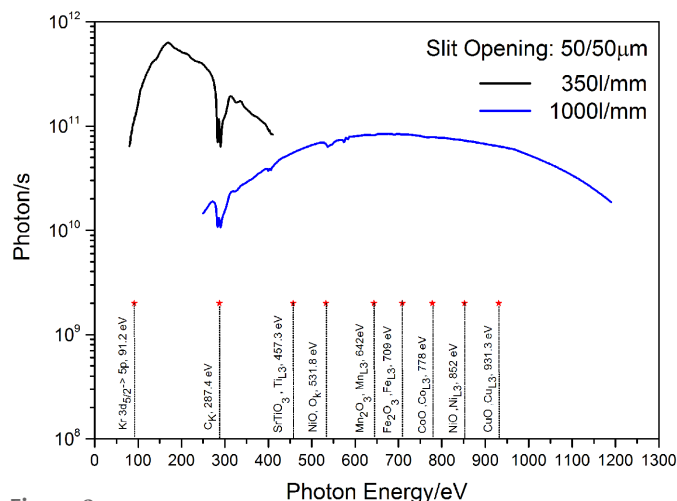


Figure 2
Photon flux measured with a photo-diode (IRD AXUV 100) normalized with the quantum efficiency of the photo-diode and the storage ring current. The photon energy was calibrated with photoionization spectra of gaseous and standard samples.

normalized with the quantum efficiency of the photo-diode and the storage ring current (360 mA, top-up mode). Two gratings (350 and 1000 grooves mm^{-1}) deliver maximum fluxes of 5×10^{11} and 8×10^{10} photons s^{-1} at 200 and 700 eV, respectively (with both slits set at 50 μm); two notable absorptions near 287.4 eV have gradually increased because of a deposition of carbon on the optical surfaces (Boller *et al.*, 1983; Chauvet *et al.*, 2011), despite the ultimate pressure of the grating chamber being less than 1×10^{-10} Torr. The ratio of second- to first-order intensities at different photon energies was determined from photoemission spectra of the Ag *d*-band. The results showed less than 6%, 3%, 5% and 3% at 80 eV, 120 eV, 160 eV and 280 eV, respectively (see supplementary figures). The energy range 80–1200 eV was tested with four photoionization absorption spectra (PAS) experiments with gaseous samples: Kr (91.5 eV), CO (287 eV), N₂ (401 eV) and Ne (867 eV); these experiments were performed in a windowless ion chamber with back-filled pressure from 7 to 18 mTorr (measured at the foreline). A pressure difference (10^{-3} – 10^{-7} Torr) was isolated with a capillary pumped with a turbomolecular pump (450 l s^{-1}).

In principle, the Lorentzian and Gaussian widths represent the core lifetime broadening and the beamline resolution (slit opening, slope error, aberration and misalignment), respectively. Fig. 3 shows an auto-ionization spectrum of gaseous Kr near the 3*d* level; transitions in a series from $3d_{5/2,3/2} \rightarrow np$ ($n = 5$ to 10) were observed. The first transition was simulated with a Voigt function (inset of Fig. 3), deconvoluted into correlated Lorentzian and Gaussian line shapes. The most confidently fitted results yielded FWHM of 74 meV and 34 meV, respectively. Relative to the results from an electron energy-loss spectroscopy measurement ($\sim 83 \pm 4$ meV; King *et al.*, 1977), the natural line obtained here is slightly narrower.

Fig. 4 shows the carbon core-level excitation of gaseous CO with three distinct structures: C $1s^{-1} \pi^*$ resonance, $1h-1e$ Rydberg states and $2h-2e$ doubly excited Rydberg states are clearly shown. The first vibrational transition, $\nu \rightarrow \nu' = 0$, was simulated with three Voigt functions (inset in Fig. 4), which were deconvoluted into mixed Lorentzian and Gaussian line shapes in three pairs. The fitting sequence converged at Lorentzian and Gaussian widths for $\nu' = 0, 1, 128-117$ and $35-34$ meV, respectively. In contrast with results of 110 and

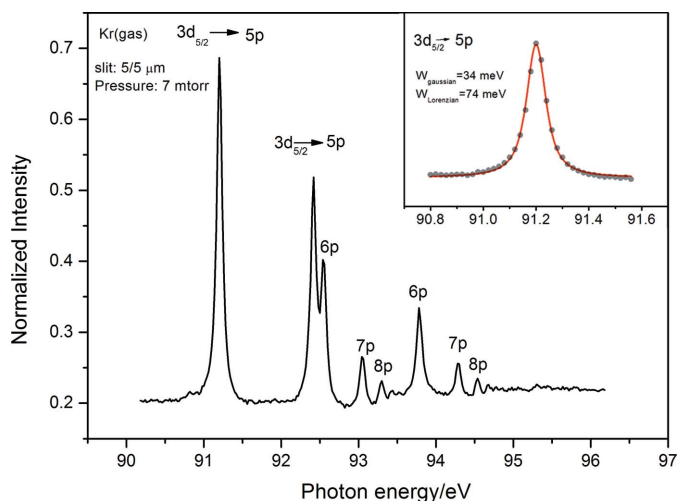


Figure 3
Photoionization spectrum of gaseous Kr, from Kr $3d_{5/2,3/2} \rightarrow np$ transition; the first transition is simulated with a Voigt line shape (inset).

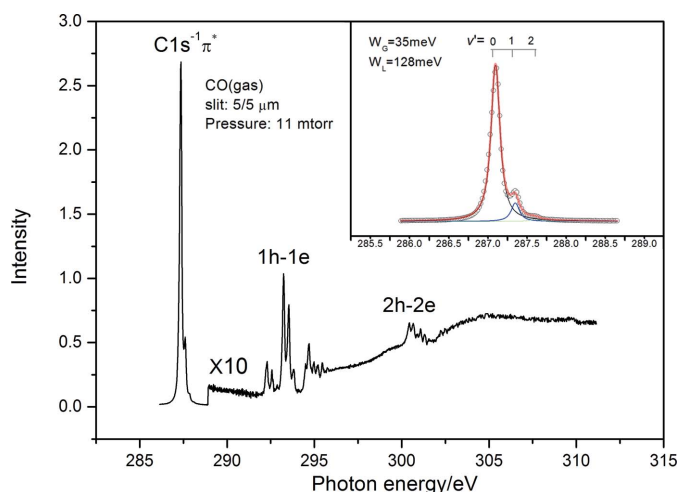


Figure 4
Carbon K -edge photoionization spectrum of gaseous CO; the inset shows the vibrational resonance transition $C 1s^{-1} \pi^*$, $\nu \rightarrow \nu = 0$ simulated with three Voigt line-shape functions.

55 meV (Domke *et al.*, 1990), minor discrepancies might be attributed to a different monochromator design and fitting algorithm.

The absorption spectrum of nitrogen at the K -edge (shown in Fig. 5) has been well known as a resolution indicator for most soft X-ray beamlines since 1989 (see Chen & Sette, 1989). Instead of using the method (sensitive to a saturation effect) of intensity ratio of the third maximum to the first minimum, the seven sub-levels of each vibrational state were fitted with a Voigt line shape after subtracting a linear background. The best-fitted widths of the first vibrational state are 127.6 and 38 meV for Lorentzian and Gaussian shapes, respectively, which are comparable with the high-performance results reported by Prince *et al.* (1999).

Fig. 6 likewise displays the core excitation of gaseous Ne; resonance states from $1s \rightarrow np$ ($n = 3, 4, 5$) are clearly shown. With the same algorithm to analyse the line shape, the Lorentzian and Gaussian widths of states $1s \rightarrow 3p$, $1s \rightarrow 4p$

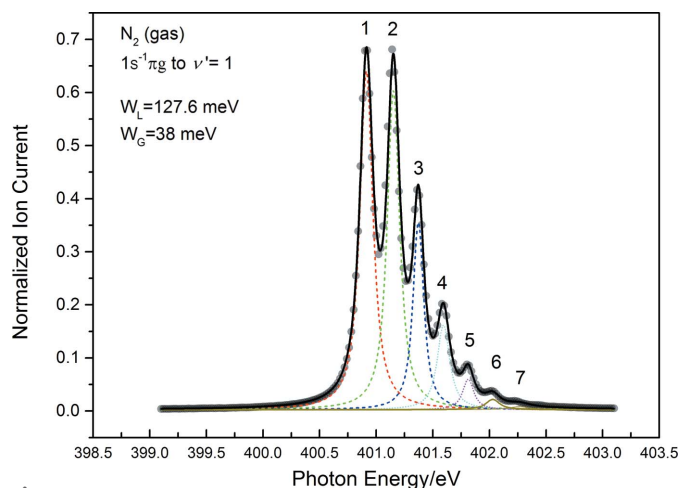


Figure 5
Nitrogen K -edge photoionization spectrum at $1s \rightarrow \pi^*$; seven vibrational sublevels of the excited state are clearly shown; each is satisfactorily fitted with a Voigt line-shape function.

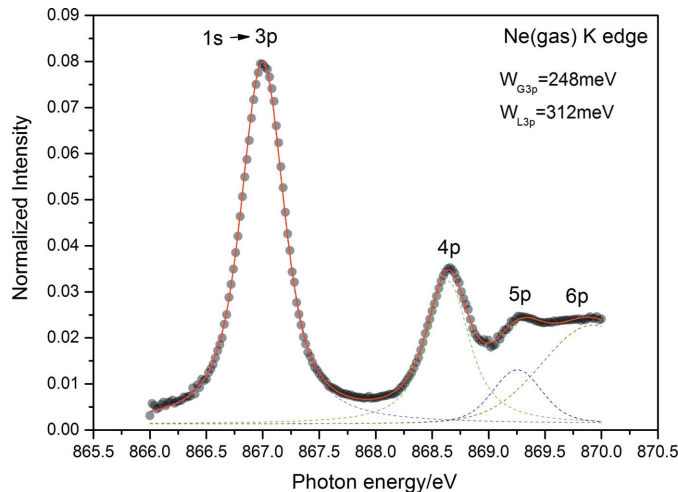


Figure 6
Neon photoionization spectra near the K -edge threshold; four transition states are simulated with three Voigt functions and a smooth step function.

are resolved (312 and 248 meV) and (350 and 208 meV), which are consistent with the results (310 and 340 meV) in the literature (Hitchcock *et al.*, 1980; Domke *et al.*, 1990).

To verify the focal position, the beam spot was sectioned in the vertical plane with a continuously moving screen along the beamline axis. Fig. 7 shows photographs of the beam profile, from 200 to 1000 eV, recorded with a digital microscope near the nominal focal position. The intensity of the greyscale for the pixels was analyzed in detail with a Gaussian line shape (Wei *et al.*, 2015). The dimensions of the beam spot at 400 eV are less than 0.55 mm vertical and 2.0 mm horizontal; both slits are set at 50 μm .

4. End-stations

The XPS end-station shown in Fig. 8(a) has been upgraded with an advanced electron spectrometer (SPECS GmbH). The electrons from a sample are collected with a magnifying lens

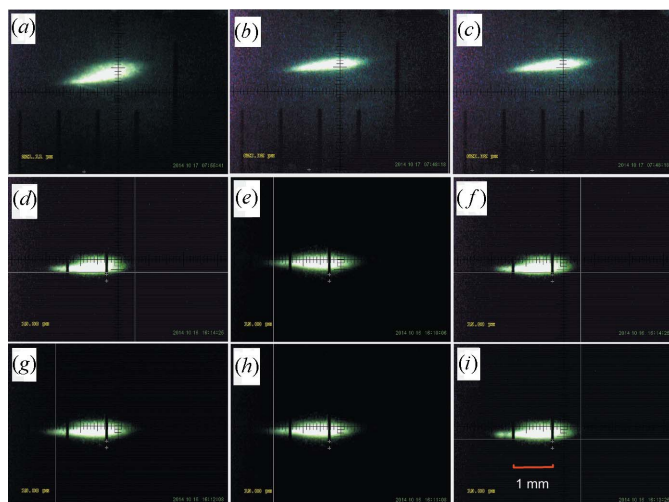


Figure 7
Photographs of the beam spot size of grating 1 at (a) 200 and (b) 400 eV, and of grating 2 at (c) 400, (d) 500, (e) 600, (f) 700, (g) 800, (h) 900 and (i) 1000 eV.

into a hemispherical energy analyser (200 mm); a multi-channel plate detector provides angular resolution 0.5° for kinetic energy over a wide range. The sample is mounted on a manipulator (CreaTec GmbH) with five degrees (x , y , z , azimuthal and polar angles) of freedom and temperature control over a wide range (100–800 K). The main chamber made of μ -metal expels a stray magnetic field that deflects the trajectory of electrons with small energy. The pumping system comprises an ion pump, a Ti sublimation pump and a turbo-

molecular pump. The base pressure routinely reaches 2×10^{-10} Torr after baking for 24 h. Multiple evaporative sources provide epitaxial deposition and low-energy electron diffraction (LEED) to test the surface ordering after a film is grown; a load-lock chamber with a transport port (6 inch) can accommodate diverse samples from millimetre to wafer size.

The XAS end-station in Fig. 8(b) is a high-throughput UHV chamber connected with a quick-entry load-lock chamber. The system is destined for research on complicated metal-oxide materials. To probe the correlated electronic properties in the bulk, detection is available in two modes for total electron yield and fluorescence yield. The manipulator with two rotational degrees of freedom of the sample provides a polarization dependence to distinguish the spin state of the electrons. The sample can be varied from 6 to 800 K with an open-cycle cryogenic cold finger and liquid helium. Six standard oxide samples (NiO, SrTiO₃, CoO, Fe₂O₃, MnO, CuO) serve as energy reference for quantitative analysis of XAS (see bottom of Fig. 2).

The IPS end-station shown in Fig. 8(c) consists of an ultra-high-vacuum (UHV) chamber equipped with a closed-cycle helium cryostat. The pressure in the UHV chamber can attain 1×10^{-10} Torr. The cold finger is mounted on the tip of the cryostat at which the temperature can attain 14 K, with a temperature controller (Lakeshore-331S) from 14 to 400 K and tunable heater at the tip of the cryostat. Partial pressures of gaseous mixtures are measured with a Baratron gauge (MKS 622A) in the range 0–10 Torr with an accuracy of 0.25%. The detection system consists of a mid-infrared Fourier-transform interferometric spectrometer (mid-FTIR)

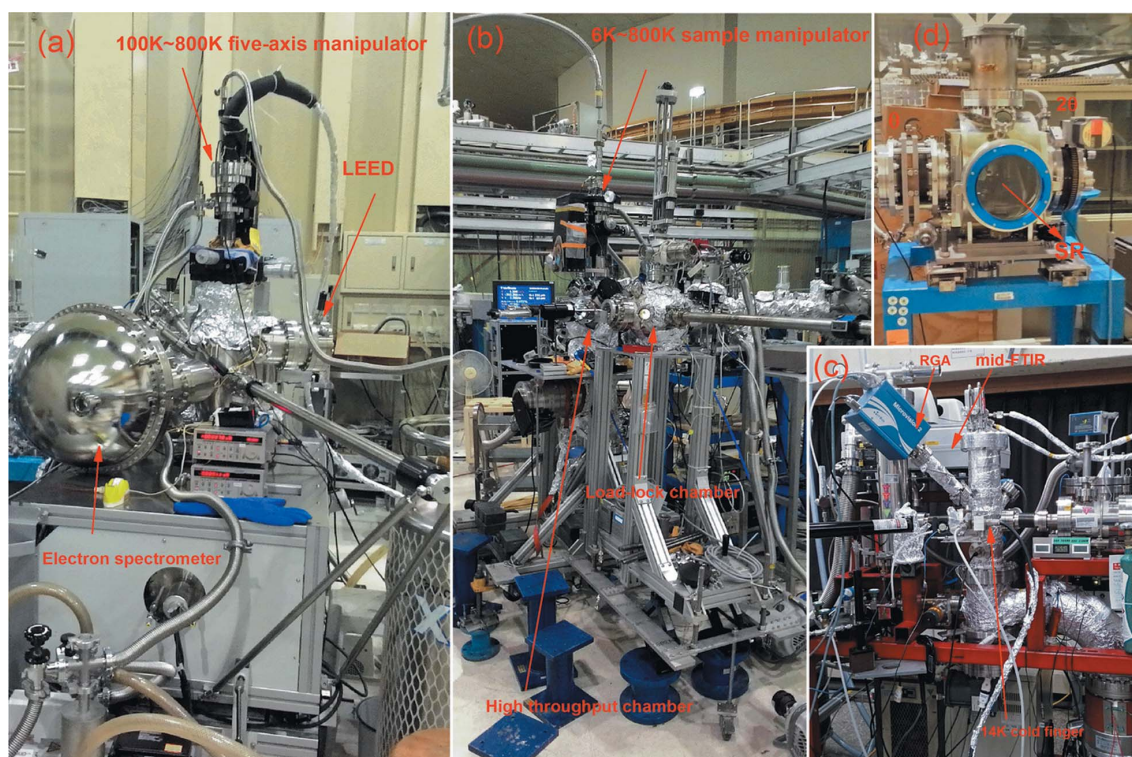


Figure 8
(a) PES end-station, (b) XAS end-station, (c) IPS end-station and (d) EUV UHV reflectometer.

and a quadrupole mass filter (MKS microvision 2). The detection limit of solid CO_2 ($2390\text{--}2300\text{ cm}^{-1}$) attains 0.1 monolayer; to monitor the sample purity and desorbed molecules, the quadrupole mass spectrometer can resolve below 0.5 unified atomic mass units upon deposition and VUV excitation.

Towards the commercial application of extreme-ultraviolet lithography (EUVL), the short life time of the multilayer-coated projection optics and the measuring of the optical properties of multilayer mirrors and photo-resists are two critical issues that remain unresolved (Thomas *et al.*, 2010; Morgan *et al.*, 2010). Fig. 8(d) shows a compact UHV reflectometer under commission at the TLS (Fu *et al.*, 2009). The chamber (8 inch) contains a goniometer for $\theta\text{--}\theta$ with a range of sample rotation from 0 to 90° and an independent range of $\theta\text{--}2\theta$ detector rotation from 0 to 180° for reflectivity measurements on multilayer samples; the angular precisions of the two driving gears are 0.001 and 0.004° , respectively. Preliminary tests at the beamline are in progress.

5. Facility access

Beam time is currently open through an application of proposal to the User Executive Committee (UEC) of NSRRC. Detailed information is available at the website <http://portal.nsrcc.org.tw/ua0/Contact/uaolist.php> or by email to the beamline spokesman (Pi@nsrcc.org.tw).

6. Highlights

In a search for primitive life origin on Earth, researchers have suggested that complicated organic substances might have been introduced *via* meteorites or comets. In experiments on the photolysis of ice, molecules such as amino acids and the nucleotide base uracil can be formed on irradiation (VUV/EUV/X-ray) of astrophysical ice; during the formation of the solar system these ices could have led to the formation of complicated organic molecules; H_2O and CH_3OH ices are the most abundant astrophysical ice components. In recent experiments at BL08B, soft X-rays were applied to interact with ice; Fig. 9 shows that newly formed species increase with the absorbed energy. Photons with energy at the oxygen edge (550 eV) produced more products than at the carbon edge (300 eV). The rate of energy deposition with broadband irradiation is more efficient than with monochromatic photons (Chen *et al.*, 2013).

Frustrated-spin materials provide a new arena in the field of magnetic ferroelectric systems; perovskite manganites such as TbMnO_3 , YMnO_3 and BiMnO_3 with T_N below 300 K have been explored extensively (Kimura *et al.*, 2003). A possible ferroelectric polarization in SmFeO_3 above 300 K has drawn attention because of its useful technical applications (Lee *et al.*, 2011; Johnson *et al.*, 2012), but the magnetic structure responsible for that ferroelectricity is difficult to observe. The misinterpretation of magnetoelastic coupling as a ferroelectric effect has been clarified (Kuo *et al.*, 2014) with X-ray magnetic linear dichroism (XMLD) at BL08B. The measurement of

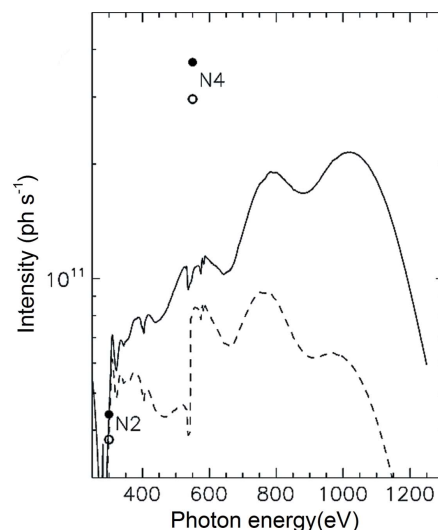


Figure 9 Black bullets and the solid curve represent measured fluxes; open circles and the dashed line are the fluxes absorbed by the ices of CH_3OH (reproduced with permission from Chen *et al.*, 2013).

polarization dependence on Fe $L_{2,3}$ XAS spectra, with the photon E-vector parallel to three orthorhombic crystal axes a , b , c (Fig. 10), shows that sufficient XMLD signals are reversed across the spin reorientation temperature T_{SR} (~ 480 K). On comparison with a simulation, the anti-

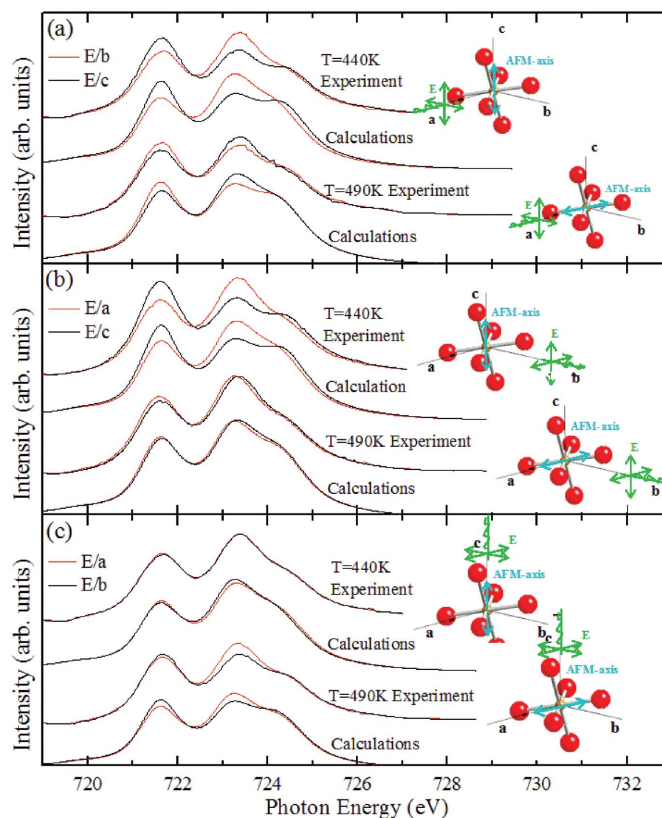


Figure 10 Polarization-dependent (incident beam parallel to axes a , b , c) XAS of the Fe $L_{2,3}$ edge of SmFeO_3 (reproduced with permission from Kuo *et al.*, 2014).

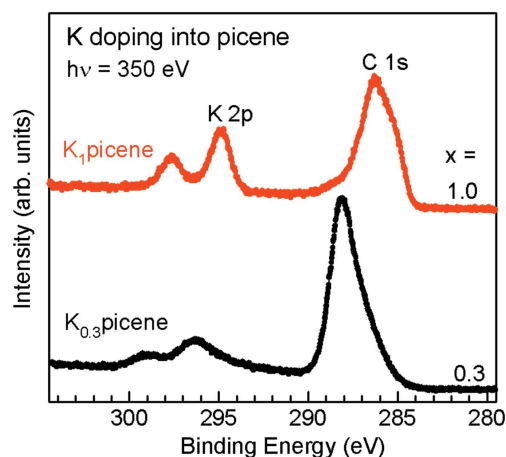


Figure 11
Stoichiometric ratio of K_x -picene determined with relative XPS signal intensities at K $2p$ and C $1s$ core levels (see also Cheng *et al.*, 2015).

ferromagnetic axes are deduced to lie in plane c - a , consistent with the result of powder neutron diffraction experiment.

XPS has provided a direct probe of the interfacial energy level of organic semiconductor devices; core-level photoelectron spectra render quantitative information to calculate the stoichiometric ratio of dopants to an organic molecule (Cheng *et al.*, 2015), for example, K $2p$ and C $1s$ core-level spectra recorded at photon energy 350 eV for a picene film doped with potassium (in Fig. 11). The stoichiometric ratio (denoted by x) of potassium to picene was deduced from relative photoelectron intensities of the K $2p$ and C $1s$ core-level signals with sensitivity factors 2.5 and 0.6, respectively; the concentration, x , of potassium atoms per picene molecule of K_x picene was thus derived.

7. Conclusion

As TLS has reached its mature stage, not only the straight sections are consumed but all bending magnet ports are unavailable. BL08B, that began as a photon-BPM sharing the front end with BL08A, is now a valuable beamline at TLS. Judging from the performance of the beamline and three mobile end-stations operated in regular beam time, there is no doubt that the upgrading plan is successful. We believe that the capability will further expand through the cooperation of multi-disciplinary users with efficient end-stations and an easily operable beamline. Apart from delicate optics and slits purchased from overseas suppliers, other major components of the beamline, such as a two-axis grating chamber and adjustment parts of the mirror holder, were fabricated by local

manufacturers, which might increase the capability of precise machinery and beamline technologies in TLS.

Acknowledgements

We acknowledge Mr Tsai-Fu Lin, Mr Chin-Yen Liu and Mr Jwei-Ming Juang for their assistance in facilitating the interlock and utilities system. The contribution of Dr King-Long Tsang (1949–2007) who first initiated the project should be memorable.

References

- Boller, K., Haelbich, R.-P., Hogrefe, H., Jark, W. & Kunz, C. (1983). *Nucl. Instrum. Methods Phys. Res.* **208**, 273–279.
- Chauvet, C., Polack, F., Silly, M. G., Lagarde, B., Thomasset, M., Kubsy, S., Duval, J. P., Risterucci, P., Pilette, B., Yao, I., Bergeard, N. & Sirotti, F. (2011). *J. Synchrotron Rad.* **18**, 761–764.
- Chen, C. T. & Sette, F. (1989). *Rev. Sci. Instrum.* **60**, 1616–1621.
- Chen, Y.-J., Ciaravella, A., Muñoz Caro, G. M., Cecchi-Pestellini, C., Jiménez-Escobar, A., Juang, K.-J. & Yih, T.-S. (2013). *Astrophys. J.* **778**, 162–173.
- Cheng, C.-P., Lu, M.-H., Chu, Y.-Y., Wei, C.-H. & Pi, T.-W. (2015). *J. Appl. Phys.* **117**, 015501.
- Domke, M., Xue, C., Puschmann, T., Mandel, T., Hudson, E., Shirley, D. A. & Kaindl, G. (1990). *Chem. Phys. Lett.* **173**, 122–128.
- Fu, H.-W., Huang, L. J., Chang, C. F., Liu, C. Y., Lin, S. W., Luo, S. W. & Fung, H. S. (2009). Technical Report TR00062. NSRRC, Hsinchu, Taiwan.
- Fung, H. S., Yuh, J. Y., Huang, L. J., Tseng, T. C., Perng, S. Y., Wang, D. J., Tsang, K. L. & Chung, S. C. (2007). *AIP Conf. Proc.* **879**, 563–566.
- Hitchcock, A. P. & Brion, C. E. (1980). *J. Phys. B*, **13**, 3269–3273.
- Hulbert, S. L., Holly, D. J., Middleton, F. H. & Wallace, D. J. (1990). *Nucl. Instrum. Methods Phys. Res. A*, **291**, 343–347.
- Johnson, R. D., Terada, N. & Radaelli, P. G. (2012). *Phys. Rev. Lett.* **108**, 219701.
- Kimura, T., Goto, T., Shintani, H., Ishizaka, K., Arima, T. & Tokura, Y. (2003). *Nature (London)*, **426**, 55–58.
- King, G. C., Read, F. H. & Tronc, M. (1977). *Chem. Phys. Lett.* **52**, 50–54.
- Kuo, C.-Y. *et al.* (2014). *Phys. Rev. Lett.* **113**, 217203.
- Lee, J.-H., Jeong, Y. K., Park, J. H., Oak, M.-A., Jang, H. M., Son, J. Y. & Scott, J. F. (2011). *Phys. Rev. Lett.* **107**, 117201.
- Morgan, C. G., Naulleau, P. P., Rekawa, S. B., Denham, P. E., Hoef, B. H., Jones, M. S. & Vane, R. (2010). *Proc. SPIE*, **7636**, 76361Q.
- Prince, K. C., Vondráček, M., Karvonen, J., Coreno, M., Camilloni, R., Avaldi, L. & de Simone, M. (1999). *J. Electron Spectrosc. Relat. Phenom.* **101–103**, 141–147.
- Thomas, P., Yankulin, L., Khopkar, Y., Garg, R., Mbanaso, C., Antohe, A., Fan, Y., Denbeaux, G., Aouadi, S., Jindal, V. & Wüest, A. (2010). *Proc. SPIE*, **7636**, 76361X.
- Tseng, P.-C., Lin, H.-J., Chung, S.-C., Chen, C.-I., Lin, H.-F., Dann, T.-E., Song, Y.-F., Hsieh, T.-F., Tsang, K.-L. & Chang, C.-N. (1995). *Rev. Sci. Instrum.* **66**, 1658–1660.
- Wei, C.-H., Lin, H.-C., Lin, S.-W. & Yuh, J.-Y. (2015). *J. Synchrotron Rad.* **22**, 1289–1292.